Tracing magnetic separators and their dependence on IMF clock angle in global magnetospheric simulations

C. M. Komar,[1] P. A. Cassak,[1] J. C. Dorelli,[2] A. Glocer,[2] and M. M. Kuznetsova[2]

[1]   A new, efficient, and highly accurate method for tracing magnetic separators in global magnetospheric simulations with arbitrary clock angle is presented. The technique is to begin at a magnetic null and iteratively march along the separator by finding where four magnetic topologies meet on a spherical surface. The technique is verified using exact solutions for separators resulting from an analytic magnetic field model that superposes dipolar and uniform magnetic fields. Global resistive magnetohydrodynamic simulations are performed using the three-dimensional Block-Adaptive Tree Solar-wind Roe-type Upwind Scheme code with a uniform resistivity, in eight distinct simulations with interplanetary magnetic field (IMF) clock angles ranging from 0° (parallel) to 180° (antiparallel). Magnetic nulls and separators are found in the simulations, and it is shown that separators traced here are accurate for any clock angle, unlike the last closed field line on the Sun-Earth line that fails for southward IMF. Trends in magnetic null locations and the structure of magnetic separators as a function of clock angle are presented and compared with those from the analytic field model. There are many qualitative similarities between the two models, but quantitative differences are also noted. Dependence on solar wind density is briefly investigated.

1. Introduction

[2]   Many important dynamic processes in the Earth's magnetosphere are known or thought to be driven by magnetic reconnection, from solar wind-magnetosphere coupling [*Gonzalez*, 1990; *Borovsky*, 2008], to magnetospheric convection [*Dungey*, 1961], to substorm phenomena [*Angelopoulos et al.*, 2008, and references therein]. Determining where reconnection happens as a function of solar wind conditions is critical for predicting its efficiency and for informing satellites, such as NASA's upcoming Magnetospheric Multiscale (MMS) mission [*Burch and Drake*, 2009; *Moore et al.*, 2013], where to expect reconnection events to occur.

[3]   In the classical model by *Dungey* [1961, 1963], reconnection occurs at the subsolar point for southward interplanetary magnetic field (IMF) and near the polar cusps for northward IMF. However, much less is known about where reconnection occurs for arbitrary IMF clock angles θ_{IMF}. For arbitrary θ_{IMF}, reconnection is likely to occur along the magnetic separator, the magnetic field line that connects magnetic nulls (where the magnetic field strength $|\mathbf{B}| = 0$) and separates regions of differing magnetic topologies [*Cowley*, 1973; *Siscoe*, 1987; *Lau and Finn*, 1990; *Siscoe et al.*, 2001]. The topology of a magnetic field line is determined by where it maps relative to Earth: closed field lines map to the Earth in both directions, open field lines do not map to Earth in either direction, and half-open field lines only map to Earth in one direction. The magnetic separator marks where magnetic topology changes, and the line integral of the parallel electric field $E_{\parallel}$ along the separator has been shown to be the global reconnection rate [*Siscoe et al.*, 2001].

[4]   A number of methods have been developed to locate magnetic separators. The eigenvectors of the 3×3 $\nabla \mathbf{B}$ tensor at a magnetic null determine the local magnetic field geometry [*Greene*, 1988; *Lau and Finn*, 1990; *Parnell et al.*, 1996]. Other methods determine the magnetic separator globally. One method convects solar wind field lines earthward to determine the separatrix surfaces [*Dorelli et al.*, 2007; *Ouellette et al.*, 2010]. The last closed field line along the Sun-Earth line has also been used as an approximation of the separator, as this field line closely approaches the magnetic nulls in global magnetospheric simulations (*Dorelli et al.* [2007] used this method for northward IMF; *Hu et al.* [2009] determined the separator for northward and southward IMF). The separator has also been located by

[1]Department of Physics and Astronomy, West Virginia University, Morgantown, West Virginia, USA.

[2]NASA Goddard Space Flight Center, Greenbelt, Maryland, USA.

Corresponding author: C. M. Komar, Department of Physics and Astronomy, West Virginia University, White Hall, Box 6315, Morgantown, WV 26506, USA. (ckomar@mix.wvu.edu)

finding where different magnetic topologies meet [*Laitinen et al.*, 2006, 2007; *Dorelli and Bhattacharjee*, 2008, 2009]. *Haynes and Parnell* [2010] developed an iterative technique to map the separator using rings along the separatrix eigenvectors of the ∇**B** tensor. Another study [*Moore et al.*, 2008] inferred reconnection geometries from deflections in streamlines at the magnetopause. A few of these studies have investigated separators as a function of IMF clock angle [*Laitinen et al.*, 2007; *Hu et al.*, 2009; *Ouellette et al.*, 2010].

[5] Magnetic nulls and separators arise in other contexts, as well. *Longcope* [1996] mapped magnetic separators in simulations of the solar corona by interpolating between the calculated separatrix surfaces at both nulls. *Close et al.* [2004] traced magnetic separators by locating changes in magnetic connectivity near magnetic nulls resulting from magnetic potential fields in solar atmospheric simulations. There has been observational evidence of magnetic nulls and separators in Earth's magnetotail [*Xiao et al.*, 2006, 2007]. Detecting these structures observationally is difficult because multiple spacecraft are needed.

[6] In this paper, we present a simple, efficient, and accurate algorithm to map magnetic separators in global magnetospheric simulations at the dayside magnetopause for arbitrary IMF clock angle. We verify the technique using exact solutions for an analytic model involving the superposition of uniform and dipolar magnetic fields. Then, we trace separators in global magnetohydrodynamic (MHD) simulations for various IMF clock angles and show that the last closed field line does not map the separators for southward IMF. We discuss trends in magnetic null locations and magnetic separators, making comparisons to the analytical field model.

[7] The layout of the paper is as follows. In section 2, we present and verify the new method for tracing magnetic separators. In section 3, we describe the global magnetospheric simulations, including a careful discussion about numerical versus explicit dissipation. The results of finding null locations and tracing separators for different IMF clock angles are discussed in section 4. The results are summarized, and potential applications are discussed in section 5. The properties of magnetic reconnection at the separators is outside the scope of the present study.

2. A Technique for Finding Separators

2.1. Technique Description

[8] The separator tracing algorithm exploits the fact that magnetic nulls are the endpoints of magnetic separators. A schematic diagram of the tracing process is shown in Figure 1. The two magnetic nulls are found using existing techniques, represented by (red) X's at the endpoints. A hemisphere, represented by a dashed semicircle, is centered around the northern null, labeled 0 (the choice of starting null is arbitrary). At many points on the hemisphere's surface, the magnetic field is traced in both directions to determine its topology (open, closed, or half-open). The point at which all topologies meet is where the separator intersects the hemisphere; we mark this intersection with a (blue) x and label it location 1. A new hemisphere is centered at location 1, and the separator's intersection with this new hemisphere is determined similarly. This new intersec-
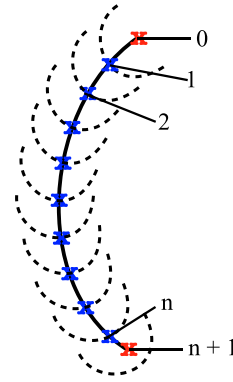
**Figure 1.** Schematic diagram of the separator tracing algorithm.

tion is marked by another (blue) x, labeled as location 2. This process is repeated until the southern null, labeled n + 1, is inside a hemisphere. The separator is mapped by connecting the nulls to the individual separator locations in order (0 through n + 1), sketched as the solid (black) line. (Note that an alternate algorithm would be to initially find a single null and perform the above iterative procedure while checking inside each hemisphere for another null at each step, but we do not pursue this further.)

[9] We now provide a more detailed description of the steps in this technique. To locate the magnetic nulls, we use the method described by *Haynes and Parnell* [2007]. Since global minima of the magnetic field magnitude |**B**| do not faithfully locate magnetic nulls, every grid cell where all three components of the magnetic field change sign is flagged. The field is then linearized within these flagged cells, and a Newton-Raphson iteration algorithm is used to locate magnetic nulls at subgrid resolution.

[10] In most of our global magnetospheric MHD simulations, to be described in section 3, this method returns a single northern null and southern null. In one, multiple nulls are identified, though the nulls in each hemisphere are within 0.25 Earth radii (R_E) of each other. To choose a null, we select the location with the lowest |**B**| in one of the hemispheres. The simulations have a high degree of symmetry, so the null in the opposite hemisphere is chosen to be closest to the null's reflection. (That is, for a null located at (*x*, *y*, *z*), the reflected null is near (*x*, –*y*, –*z*)). The null identification is verified by plotting field lines in the vicinity of the chosen nulls; magnetic fields with different topologies converge in these regions, as expected.

[11] Having identified the nulls, we proceed to map the separator. Each hemisphere in the iteration has a fixed radius R_{HS} (hemispheres are used to automatically prevent retracing in the opposite direction). Points on the hemisphere's surface are mapped by a set of angular coordinates (ϕ, λ), where ϕ is the longitude measured from the +*x* axis in geocentric solar ecliptic (GSE) coordinates and λ is the latitude (in GSE coordinates, *x* is sunward, *y* is duskward, and *z* is northward). In spherical coordinates, $\lambda = 90° – \theta$, where θ is the polar angle measured from the +*z* axis in GSE.

[12] We use hemispheres with a radius of 1 R_E, and the surface of each hemisphere is discretized into a $N_\phi \times N_\lambda$ grid and the topology of the magnetic field is determined at each grid point (we use a 61 × 61 grid). To calculate magnetic
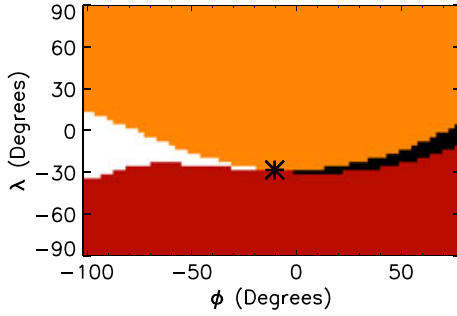
Figure 2. Sample topology map for $\theta_{\mathrm{IMF}} = 30°$ for a hemisphere centered at $\mathbf{r} = (3.16,\ 1.87,\ 8.01)\ R_E$, with radius of $1\ R_E$. Colors denote magnetic topology: red are the closed terrestrial fields, orange are the open solar wind fields, black and white are the half-closed fields that map to the south and north poles of Earth, respectively. The black asterisk marks the approximate separator location.

topology, we use the Kameleon software package developed at NASA's Community Coordinated Modeling Center (CCMC). We perform a bidirectional trace of the magnetic field at each point on the surface, using the field's footpoints to determine its topology. A field line is closed if both footpoints are within $5\ R_E$ of the origin and is open if both do not. Half-closed field lines have one footpoint within $5\ R_E$ of the origin. If the footpoint close to the origin has a negative z coordinate, then the field line is a southern half-closed field line. Conversely, a northern half-closed field line has the connecting footpoint with a positive z coordinate. Each point on the hemisphere is coded by its topology. An example is in Figure 2; closed magnetic fields are colored red, open magnetic fields are orange, southern half-closed fields are black, and northern half-closed fields are white.

[13] To identify where the four topologies meet, interpolation is usually necessary. The separator lies in between the northern and southern half-closed regions. We start by searching through the topological map for the locations where these regions are closest. In Figure 2, the two closest points are at $(0°, -30°)$ and $(-20°, -28°)$. We find the topology of the field line through the midpoint of the line connecting these points. Then, we march out along the line perpendicular to this line until the topology changes. The separator location is defined as the average of the two points with differing topologies. Figure 2 displays a (black) asterisk at its approximate separator location which reasonably estimates where the four topologies meet.

[14] The separator location is used as the center of the subsequent hemisphere. If the separator intersects the kth hemisphere at longitude and latitude $(\phi_k,\ \lambda_k)$, the coordinates of the next hemisphere's center $\mathbf{r}_{k+1}$ are

$$\mathbf{r}_{k+1} = \mathbf{r}_k + \mathbf{r}(R_{\mathrm{HS}},\ \phi_k,\ \lambda_k), \qquad (1)$$

where $\mathbf{r}_k$ is the center of the kth hemisphere, and $\mathbf{r}(R_{\mathrm{HS}}, \phi_k, \lambda_k)$ is the separator's location on the kth hemisphere in spherical coordinates relative to $\mathbf{r}_k$. A range of $[\phi_k - 90°,\ \phi_k + 90°]$ is used as the longitude of $(k + 1)$st hemisphere; this explains why the horizontal axis in Figure 2 is not centered around $\phi = 0°$. An arbitrary degree of accuracy can be obtained by decreasing the radius R_{HS}

and/or increasing the number of grid points N_ϕ, N_λ on the hemispheres.

[15] The method described here has some similarities to the four field junction method by *Laitinen et al.* [2006]. This method calculates the magnetic topology at every point on a Cartesian grid near regions where the separator is thought to exist. The separator is approximated by locations where all four topologies are within three grid cells of each other, resulting in a ribbon-like structure at the dayside magnetopause. Our method does not require a priori knowledge of the separator's location, as it starts from the nulls and traces the complete separator. It is also computationally inexpensive, since the magnetic topology is calculated on a number of surfaces rather than a volume at the dayside magnetopause.

2.2. Verification With Vacuum Superposition

[16] To test the technique in section 2.1, we use a simple magnetic field model with analytic solutions for the nulls and separators. We superpose a dipolar magnetic field $\mathbf{B}_D$ with a uniform background magnetic field $\mathbf{B}_{\mathrm{IMF}}$. The vacuum superposition magnetic field $\mathbf{B}_{\mathrm{VS}}$ is given by

$$\mathbf{B}_{\mathrm{VS}}(\mathbf{r}) = \mathbf{B}_D(\mathbf{r}) + \mathbf{B}_{\mathrm{IMF}}, \qquad (2)$$

where

$$\mathbf{B}_D(\mathbf{r}) = \frac{3(\mathbf{M} \cdot \hat{\mathbf{r}})\hat{\mathbf{r}} - \mathbf{M}}{r^3}, \qquad (3)$$

$\mathbf{M}$ is the Earth's magnetic dipole moment, and $\mathbf{r}$ is the position vector. The IMF in GSE coordinates is

$$\mathbf{B}_{\mathrm{IMF}} = B_{\mathrm{IMF}}\left(\sin\theta_{\mathrm{IMF}}\ \hat{\mathbf{y}} + \cos\theta_{\mathrm{IMF}}\ \hat{\mathbf{z}}\right), \qquad (4)$$

where $B_{\mathrm{IMF}} = |\mathbf{B}_{\mathrm{IMF}}|$ and θ_{IMF} is the clock angle that the IMF makes with the z axis. The positions $\mathbf{r}_{\mathrm{Null}}$ of the magnetic nulls satisfy

$$\mathbf{B}_D(\mathbf{r}_{\mathrm{Null}}) + \mathbf{B}_{\mathrm{IMF}} = 0. \qquad (5)$$

For the chosen form of $\mathbf{B}_{\mathrm{IMF}}$ and using no dipole tilt, the nulls in spherical coordinates are at $\mathbf{r}_{\mathrm{Null}} = (r_{\mathrm{Null}},\ \phi_{\mathrm{Null}} = \pm 90°,\ \pm\lambda_{\mathrm{Null}})$ [*Yeh*, 1976; *Hu et al.*, 2009], where

$$r_{\mathrm{Null}} = \left(\frac{M}{2B_{\mathrm{IMF}}}\right)^{1/3}\left[\cos\theta_{\mathrm{IMF}} + \sqrt{8 + \cos^2\theta_{\mathrm{IMF}}}\right]^{1/3} \qquad (6)$$

and

$$\lambda_{\mathrm{Null}} = \tan^{-1}\left(\frac{3\cos\theta_{\mathrm{IMF}} + \sqrt{8 + \cos^2\theta_{\mathrm{IMF}}}}{4\sin\theta_{\mathrm{IMF}}}\right). \qquad (7)$$

In GSE coordinates, $\mathbf{r}_{\mathrm{Null}} = (x_{\mathrm{Null}},\ y_{\mathrm{Null}},\ z_{\mathrm{Null}})$ with

$$x_{\mathrm{Null}} = 0, \qquad (8)$$

$$y_{\mathrm{Null}} = r_{\mathrm{Null}}\left(\frac{3 + \sin^2\theta_{\mathrm{IMF}} - \cos\theta_{\mathrm{IMF}}\sqrt{\cos^2\theta_{\mathrm{IMF}} + 8}}{6}\right)^{1/2}, \qquad (9)$$

and

$$z_{\mathrm{Null}} = r_{\mathrm{Null}}\left(\frac{2 + \cos^2\theta_{\mathrm{IMF}} + \cos\theta_{\mathrm{IMF}}\sqrt{\cos^2\theta_{\mathrm{IMF}} + 8}}{6}\right)^{1/2}. \qquad (10)$$

The nulls lie in the dawn-dusk plane ($x = 0$), as there is no B_x component to the IMF. The separator is a semicircular arc of radius r_{Null} connecting the two nulls [*Cowley*, 1973; *Yeh*, 1976; *Hu et al.*, 2009]. To motivate that this is the case, note that for pure southward B_{IMF}, the separator is a circle
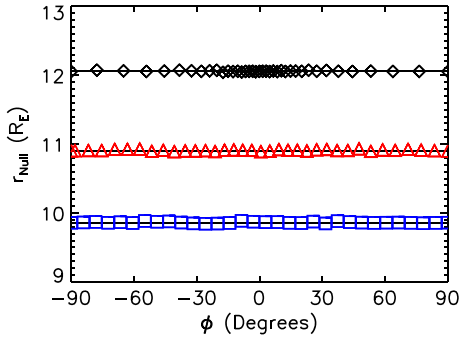
Figure 3. Verification of the separator tracing algorithm for $\theta_{\text{IMF}} = 30°$ (black diamonds), 90° (red triangles), and 150° (blue squares) using vacuum superposition. The exact solutions for the separator are shown as solid (black) lines.

in the ecliptic plane. For other clock angles, the separator rotates out of the ecliptic plane by λ_{Null} without changing its shape.

[17] We use the technique from section 2.1 to trace separators in vacuum superposition with $\theta_{\text{IMF}} = 30°$, 90°, and 150° for a system with $\mathbf{M} = -5.13 \times 10^4$ nT R_E^3 $\hat{\mathbf{z}}$ and $B_{\text{IMF}} = 56$ nT. The tracing algorithm uses hemispheres with radii $R_{\text{HS}} = 1$ R_E. The separator locations are plotted in Figure 3 as (black) diamonds for $\theta_{\text{IMF}} = 30°$, (red) triangles for 90°, and (blue) squares for 150°. The exact solutions for the separator from equation (6) are plotted as solid (black) lines. The measured separator locations agree exceedingly well with the exact solutions.

[18] To test the accuracy of the algorithm, we repeat the tracing using hemispheres with radii $R_{\text{HS}} = 5$ R_E (not shown). As expected, the agreement is better with hemispheres of smaller radii. The scatter of the separator locations from the exact solution in equation (6), measured as the average absolute difference between the measured separator radius and r_{Null}, is $\sim 75\%$ lower when smaller hemispheres are used.

3. Magnetospheric Simulation Study

3.1. The Code and its Initialization

[19] To find separators on a self-consistently generated magnetosphere, global simulations using the Block-Adaptive Tree Solar-wind Roe-type Upwind Scheme (BATS-R-US [*Powell et al.*, 1999; *Gombosi et al.*, 2000; *De Zeeuw et al.*, 2000] are performed at NASA's CCMC. BATS-R-US solves the MHD equations on a three-dimensional rectangular irregular grid. The simulation domain is $-255 < x < 33$, $-48 < y < 48$, and $-48 < z < 48$, where distances are measured in R_E and the coordinate system is GSE.

[20] The simulations are run using BATS-R-US version 8.01 and do not use the Rice Convection Model. The simulations are evolved for 2 h (02:00:00) of magnetospheric time. We look at the 02:00:00 mark of simulation data because the system has achieved a quasi-steady state; the magnetopause current layer along the x axis is approximately stationary. The standard high-resolution grid for CCMC simulations has 1,958,688 grid cells with a coarse resolution of 8 R_E in the far magnetotail, and a fine resolution of 0.25 R_E near the magnetopause. The present study employs a higher

resolution grid of 0.125 R_E packed in the region $-6 < x < 10$, $-10 < y < 10$, and $-5 < z < 5$ R_E with 3,736,800 total grid cells.

[21] The simulations do not employ a dipole tilt and use fixed solar wind inflow conditions. The solar wind has temperature $T = 232,100$ K, IMF strength 20 nT, number density $n = 20$ cm^{-3}, and a solar wind velocity of $\mathbf{v} = -400$ km/s $\hat{\mathbf{x}}$. We perform distinct simulations with IMF clock angle $\theta_{\text{IMF}} = 0°$ (parallel), 30°, 60°, 90°, 120°, 150°, 165°, and 180° (antiparallel). The IMF does not have a B_x component. Constant Pederson and Hall conductances of 5 mho are used. The solar radio flux F10.7 index is set at a value of 150.

### 3.2. Numerical Versus Explicit Dissipation

[22] Many global MHD simulations use numerical grid-scale dissipation instead of explicit dissipation because the latter is unnecessary for large-scale physics and can even be detrimental [*Raeder*, 1999]. However, explicit dissipation is essential for studies involving magnetic reconnection and magnetic topology. For example, global simulations revealed plasma flows through the reconnection X-line [*Siscoe et al.*, 2002; *Dorelli et al.*, 2004]; some researchers believed this to be spurious due to high dissipation, but later studies showed this flow is a fundamental aspect of asymmetric reconnection [*Cassak and Shay*, 2007, 2009].

[23] For the present simulations, we employ a uniform explicit resistivity η. It is known that the magnetosphere is not collisional, but including an explicit resistivity allows for reproducible results that are independent of the numerics. We include an explicit resistivity $\eta/\mu_0 = 6.0 \times 10^{10}$ m^2/s in our simulations. To ensure this resistivity controls the dissipation instead of the numerics, we show J_y in the $y = 0$ plane at the dayside magnetopause in Figure 4 for (a) no explicit resistivity and (b) with the explicit resistivity. The current layer broadens from six cells to eight cells across, suggesting the explicit resistivity is controlling the dissipation, as desired. This explicit resistivity is similar to the value obtained in a recent study that determined the size of the resistivity necessary for it to control the dissipation (G. Toth, private communication, 2010).

[24] To facilitate comparisons with previous simulations, we estimate a Lundquist number $S = \mu_0 c_A L/\eta$ for the explicit resistivity simulation with $\theta_{\text{IMF}} = 180°$. We base the length scale L on the half-length of the reconnecting current sheet in the outflow direction (as opposed to a global length scale), which is 5.35 R_E. For the Alfvén speed c_A, we use a hybrid magnetosheath/magnetospheric value c_{Ah} based on the asymmetric reconnection theory of *Cassak and Shay* [2007] of the form

$$c_{Ah}^2 \sim \frac{B_1 B_2 (B_1 + B_2)}{\mu_0 (\rho_1 B_2 + \rho_1 B_2)}, \qquad (11)$$

where B and ρ are the magnetic fields and plasma densities measured upstream of the current layer, and subscripts "1" and "2" indicate quantities measured in the magnetosphere and magnetosheath. The magnetic fields and densities, measured immediately upstream of the reconnecting current sheet in the earthward and sunward directions, are $B_1 = 116$ nT, $B_2 = 90$ nT, $n_1 = 10$ cm^{-3}, and $n_2 = 57$ cm^{-3}, giving $c_{Ah} \simeq 380$ km/s. The resulting Lundquist number based on these quantities and our chosen explicit resistivity
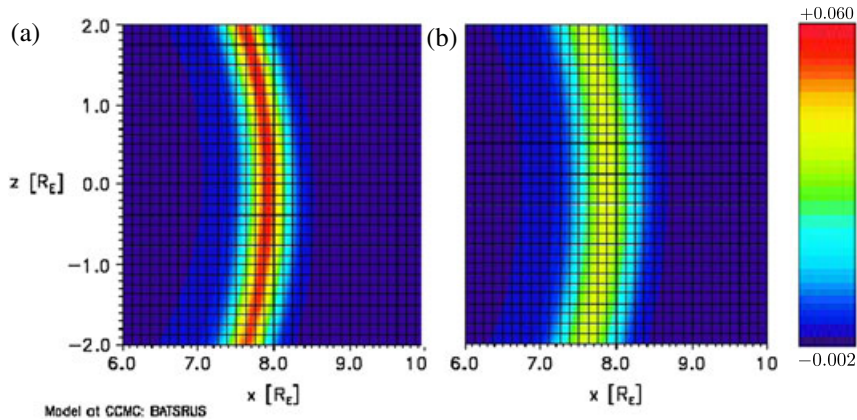
Figure 4. Magnetopause current density J_y $(\mu A/m^2)$ near the subsolar point in high-resolution simulations (a) without an explicit resistivity and (b) with an explicit resistivity $\eta/\mu_0 = 6.0 \times 10^{10}$ m^2/s. The current layer broadens in Figure 4b, demonstrating the explicit resistivity dominates numerical effects. Solid (black) lines indicate the simulation grid (0.125 R_E).

is $S \simeq 210$. A benefit of choosing the explicit resistivity this large is that the rate of production of plasmoids (i.e., flux transfer events, FTEs) is decreased. While FTEs do occur at the magnetopause, they would needlessly complicate the present fundamental physics study on field line topology.

4. Results

[25] Here we describe the results of finding nulls and tracing separators in the global, resistive MHD simulations described in section 3. To develop perspective on the results, we compare the results to nulls and separators in vacuum superposition given by equations (6) and (7). To make a careful comparison, we do not use the nominal values of $\mathbf{M} = -3.11 \times 10^4$ nT R_E^3 $\hat{\mathbf{z}}$ and $B_{IMF} = 20$ nT because the terrestrial magnetic field is enhanced due to compression by the solar wind and the IMF increases at the bow shock. We find more appropriate values from the MHD simulations. The magnetic field strengths are measured upstream of the current sheet at the subsolar point. To do so, the locations where the magnetopause current drops to $1/e$ of its maximum on the Sun-Earth line is found for both sides of the sheet. On the magnetospheric side, the magnetic field averages a 65% increase over Earth's nominal dipole field in our simulations for all clock angles, so we employ $\mathbf{M} = -5.13 \times 10^4$ nT R_E^3 $\hat{\mathbf{z}}$. On the magnetosheath side, $B_{IMF} \simeq 56$ nT for all clock angles. These are the values we employ for the vacuum superposition fields.
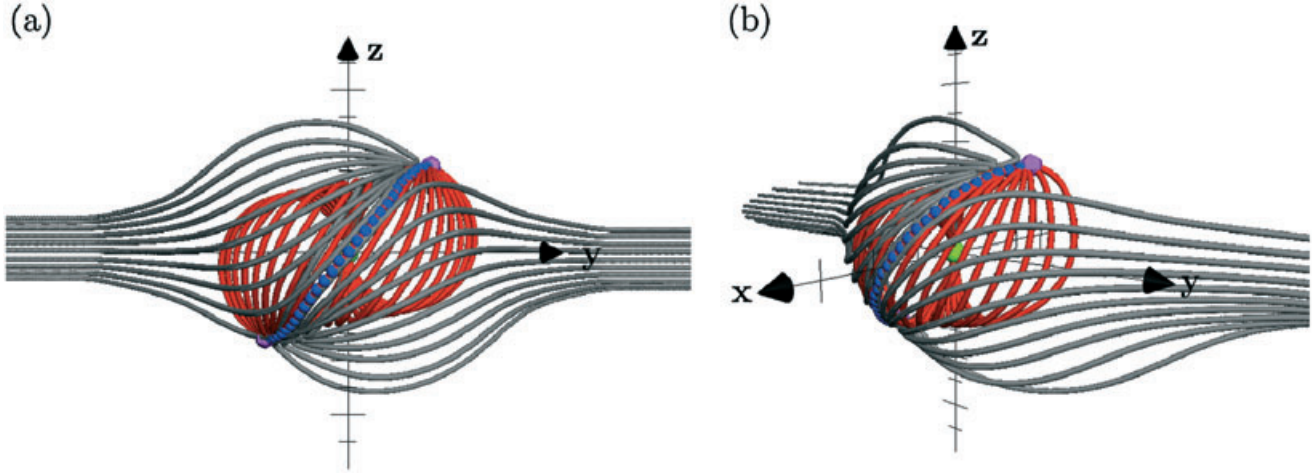
4.1. The Magnetic Nulls

[26] We find the magnetic nulls by employing the *Haynes et al.* [2007] method and their GSE locations are listed in Table 1 for the MHD simulations and for the vacuum superposition fields. The latter are in close agreement with equations (8)–(10). The measured magnetic field strength at each of the locations identified as nulls is 0.1 nT or lower. Nulls for $\theta_{IMF} = 180°$ are not reported as there are an infinite number of them in the ecliptic plane. As an example, the magnetic nulls for the $\theta_{IMF} = 90°$ MHD simulation are plotted as purple spheres in Figure 5, showing an (a) earthward and (b) oblique view for perspective. The Earth is depicted as the green sphere (to scale).

[27] The location of the magnetic nulls exhibits a few interesting trends as a function of IMF clock angle. The nulls in vacuum superposition have a range of $12.3 \geq r_{Null} \geq 9.7$ R_E for $0° \leq \theta_{IMF} \leq 180°$, whereas the nulls found in MHD have a nearly constant $r_{Null} \simeq 10.5$ R_E. The trend in r_{Null} differs because the magnetopause is located where the magnetospheric magnetic pressure balances the solar wind ram pressure in MHD. Our MHD simulations all have the same solar wind conditions, which explains why r_{Null} remains constant in MHD. Vacuum superposition is only a magnetic field model and does not capture this solar wind physics. The magnetopause shrinks as θ_{IMF} increases because the B_z component of B_{IMF} becomes increasingly negative, enabling the IMF to penetrate further into the magnetosphere.

[28] Figure 6 displays the measured MHD coordinates of the nulls as asterisks and the solid lines as the predicted values for vacuum superposition from equations (8) to (10) as a function of θ_{IMF}. The y and z coordinates of the nulls follow qualitatively similar trends for both vacuum superposition and MHD and are within 2 R_E of each other for all clock angles. In Figure 6b, the y coordinate increases from zero as θ_{IMF} increases, and the nulls move out of the noon-midnight plane. The z coordinate decreases to zero for increasing clock angle, as seen in Figure 6c. This is because the nulls are located at the magnetic cusps for northward IMF and are in the ecliptic plane for southward IMF.

Table 1. The (x, y, z) Coordinates (in GSE) of Determined Magnetic Nulls in Global Magnetosphere Simulations and in Vacuum Superposition with $\mathbf{M} = -5.13 \times 10^4$ nT R_E^3 $\hat{\mathbf{z}}$ and $B_{IMF} = 56$ nT

Clock Angle	MHD Nulls (R_E)	Vacuum Nulls (R_E)
0°	(0.08, 0.00, ±10.28)	(0.00, 0.00, ±12.24)
30°	(−0.10, ±2.99, ±9.99)	(0.00, ±4.08, ±11.34)
60°	(−0.44, ±5.19, ±9.35)	(0.00, ±7.18, ±9.06)
90°	(−0.41, ±7.70, ±7.96)	(0.00, ±8.91, ±6.29)
120°	(−0.92, ±9.55, ±5.83)	(0.00, ±9.56, ±3.78)
150°	(−2.16, ±11.03, ±3.46)	(0.00, ±9.70, ±1.75)
165°	(0.93, ±10.11, ±1.89)	(0.00, ±9.71, ±0.85)

Figure 5. Results of the present algorithm in the MHD simulation with $\theta_{\mathrm{IMF}} = 90°$ looking (a) earthward and (b) at an oblique angle for perspective. Magnetic nulls are enclosed by (purple) spheres, and Earth is the (green) sphere at the origin (to scale). The last closed magnetic field lines in the ecliptic plane are displayed in red, and adjacent half-closed topologies are displayed in gray.

[29] The x coordinates of the nulls displayed in Figure 6a do not follow the same trend as in vacuum superposition. The nulls in vacuum superposition are in the dawn-dusk plane ($x = 0$) for all θ_{IMF} as there is no B_x component of the IMF [see equation (8)]. In the MHD simulations, the nulls are near $x = 0$ for small clock angles but migrate toward the nightside as θ_{IMF} increases toward 150°. Interestingly, this trend is broken for $\theta_{\mathrm{IMF}} = 165°$ which has a null with a $+x$ coordinate.

[30] One might suggest the migration of the nulls to the nightside results from the draping of the IMF over the magnetosphere. Draping causes the IMF to be oriented sunward in the southern hemisphere and tailward in the northern hemisphere for northward IMF, with the opposite being true for southward IMF. However, this effect would make the nulls migrate opposite to the observed direction, so draping cannot explain the migration of the nulls' x coordinate. We conclude that there is no simple explanation of the trend
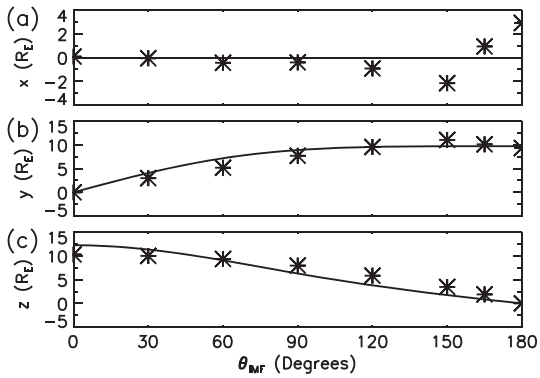
in the x coordinate of the nulls, but this is not surprising since null locations are dependent on the shape of the magnetopause, which has a multi-parameter dependence on upstream solar wind conditions [*Lu et al.*, 2011; *Liu et al.*, 2012].
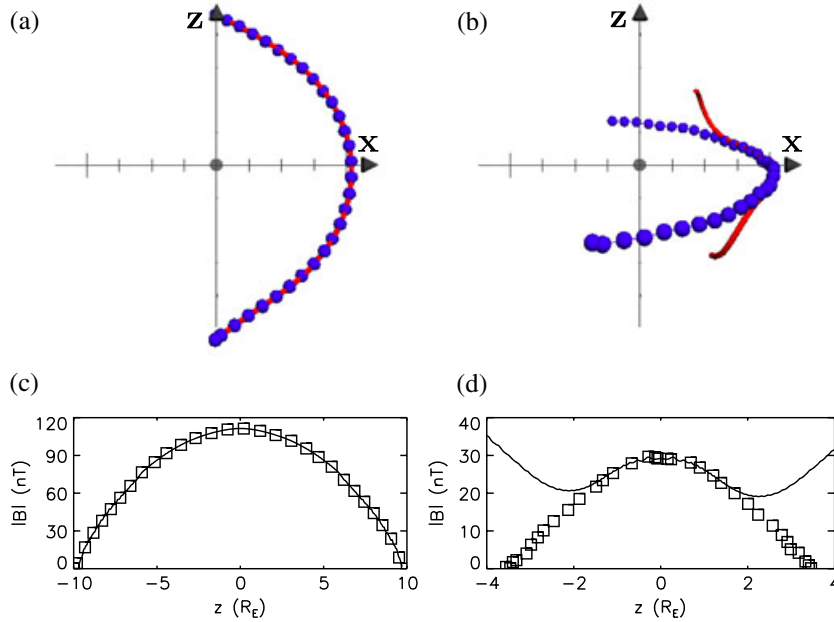
4.2. The Magnetic Separators

[31] The separator tracing method described in section 2 is used to trace the dayside separators for the MHD simulations. We start from the magnetic nulls described in the previous section and use hemispheres with radii of $R_{\mathrm{HS}} = 1 \, R_E$ to trace the separators.

[32] Care must be taken in tracing the separator for $\theta_{\mathrm{IMF}} = 180°$ due to the infinite number of nulls in the ecliptic plane. We start by centering a hemisphere at the subsolar point $\mathbf{r}_{\mathrm{Null}} = (7.87, 0.00, 0.00) \, R_E$ and the hemisphere is discretized into the same $N_\phi \times N_\lambda$ grid as described in section 2.1. The hemisphere's coordinates span longitude $0° \le \phi \le 180°$ and latitude $-90° \le \lambda \le 90°$. The chosen longitude range only traces the portion of the separator duskward of the subsolar point. The algorithm iteratively marches in the ecliptic plane until it no longer detects a merging location, ending at $\mathbf{r} = (2.93, 9.33, 0.00) \, R_E$. The dawnward portion of the separator is traced likewise by forcing the hemisphere to have a longitude range of $-180° \le \phi \le 0°$, ending at $\mathbf{r} = (2.93, -9.33, 0.00) \, R_E$. The resulting separator is stitched together with the subsolar point as the center of each portion.

[33] An example of a traced separator is shown in Figure 5, with the blue spheres denoting the intersection of the separator with the hemispheres form the iterative technique described in section 2.1. For perspective, the last closed field lines in the ecliptic plane are shown in red, and the adjacent half-closed field lines are shown in gray.

4.2.1. Comparison With the Last Closed Field Line

[34] The last closed field line on the Sun-Earth line has been used to approximate the magnetic separator since it closely approaches both magnetic nulls (northward IMF: *Dorelli et al.* [2007]; southward and northward IMF: *Hu*

Figure 6. Plots of magnetic null (a) x, (b) y, and (c) z coordinates as functions of IMF clock angle θ_{IMF}. Solid lines display vacuum superposition prediction from equations (8) to (10), and asterisks are the coordinates of nulls in the MHD simulations.

Figure 7. Comparison between traced separators and the last closed field line in global MHD simulations. The last closed field line is a solid (red) line, and the determined separator locations are (blue) spheres for θ_{IMF} of (a) 30° and (b) 150°. The magnetic field strength |**B**| as a function of z coordinate along the separator is a solid line for the last closed field line and as squares for the traced separator for θ_{IMF} (c) 30° and (d) 150°.

et al. [2009]). We compare the traced separators with the last closed field lines on the x axis for two different clock angles. Figures 7a and 7b show the last closed field line as a solid (red) line and the individual locations determined by the method described in section 2 as (blue) spheres for $\theta_{IMF} = 30°$ and 150°, respectively. The traced separator and last closed field line are nearly identical in Figure 7a, where the IMF has a northward B_z. In contrast, the two have a large deviation in Figure 7b, where the IMF has a southward B_z. Figures 7c and 7d display |**B**| as a function of separator z coordinate along the separator, with the last closed field line shown as a solid (black) line and the locations of the traced separator plotted as squares for the same two cases. The last closed field line and the traced separator are coincident in Figure 7c and, importantly, both connect with the magnetic nulls. In Figure 7d, the traced separator closely agrees with the last closed field line near the subsolar point, but only the traced separator connects with the magnetic nulls, while the last closed field line diverges strongly. More generally, we find that both methods agree near the subsolar point for all θ_{IMF}, but as θ_{IMF} increases from 90°, the last closed field line increasingly deviates from the traced separators. Therefore, the last closed field line does not accurately map the entire separator for southward B_z in our simulations. While the last closed field line is accurate for northward B_z, the method of section 2.1 works for any clock angle.

4.2.2. Clock Angle Dependence of MHD Separators
[35] We now turn to comparing separators for different clock angles. The separators traced for clock angles 30° through 180° are displayed in Figure 8. Figure 8a displays the separators looking duskward along the y axis, and Figure 8b displays the separators looking earthward along

the x axis. Each separator is roughly coplanar and is tilted around the x axis by an amount dependent on the clock angle.

[36] To quantify the structural properties of the separator, we define the separator tilt angle κ at the subsolar point measured with respect to the z axis. The tilt angles of the separators are measured using the B_y and B_z components of the last closed field line at the subsolar point:

$$\kappa_{MHD} = \tan^{-1}\left(\frac{B_y}{B_z}\right). \quad (12)$$

To investigate the separator shape as a function of clock angle, we rotate clockwise around the $+x$ axis by κ_{MHD} and display the separator's projection in this rotated plane. The
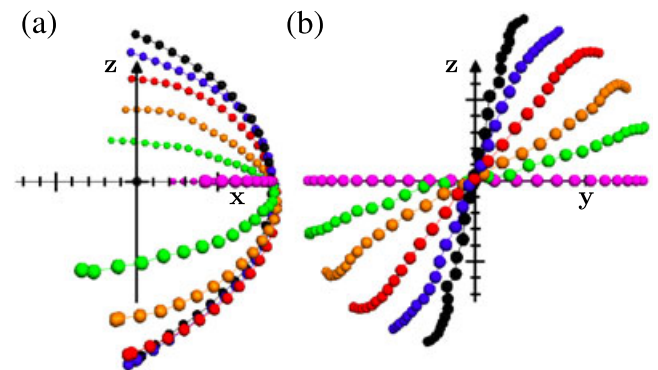
Figure 8. Plot of separators in global MHD simulations for $\theta_{IMF} = 30°$ (black), 60° (blue), 90° (red), 120° (orange), 150° (green), and 180° (purple) looking (a) duskward and (b) earthward.
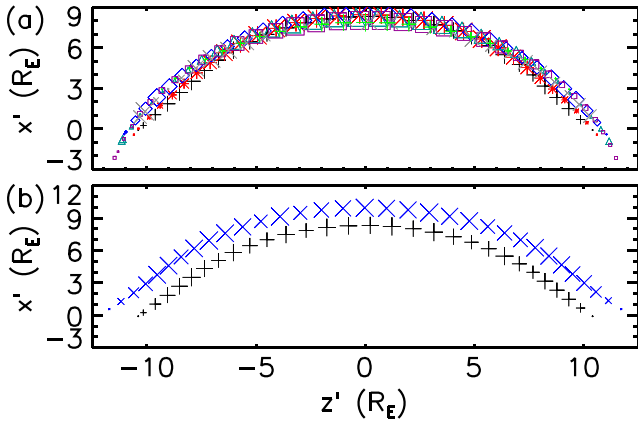
Figure 9. MHD separators rotated around $\hat{x}$ into a common plane. (a) Separators for the different clock angles are: 30° (black plus), 60° (red asterisk), 90° (blue diamond), 120° (green triangle), 150° (purple squares), 165° (grey X), and 180° (green plus). (b) Plot of MHD separators with $\theta_{IMF} = 30°$ with solar wind number density $n = 20$ cm^{-3} (black plus) and $n = 5$ cm^{-3} (blue X). Symbol size is inversely related to the deviation from the plane.

separator's projected coordinates in this plane are given by

$$\begin{pmatrix} x' \\ y' \\ z' \end{pmatrix} = \begin{pmatrix} 1 & 0 & 0 \\ 0 & \cos\kappa_{MHD} & -\sin\kappa_{MHD} \\ 0 & \sin\kappa_{MHD} & \cos\kappa_{MHD} \end{pmatrix} \begin{pmatrix} x \\ y \\ z \end{pmatrix}, \quad (13)$$

where x' points sunward, y' is the out-of-plane direction, z' is the plane of the separator, and (x, y, z) is the vector for a given location on the separator in GSE coordinates.

[37] Figure 9a shows the separator's projection in the rotated plane for different IMF clock angles: $\theta_{IMF} = 30°$ as (black) pluses ($\kappa_{MHD} \simeq 12.6°$), 60° as (red) asterisks ($\kappa_{MHD} \simeq 21.4°$), 90° as (blue) diamonds ($\kappa_{MHD} \simeq 40.2°$), 120° as (green) triangles ($\kappa_{MHD} \simeq 62.8°$), 150° as (purple) squares ($\kappa_{MHD} \simeq 79.4°$), 165° as (gray) X's ($\kappa_{MHD} \simeq 79.0°$), and 180° as (green) pluses ($\kappa_{MHD} = 90°$). The symbol size denotes the location's deviation from the plane, with smaller symbols indicating a larger deviation from the plane.

[38] Figure 9a simultaneously quantifies three structural features of the magnetic separators. It is clearly seen that the separators maintain a similar shape regardless of θ_{IMF}. Also, the separators rotate around the magnetopause for increasing θ_{IMF}, turning clockwise around the $+x$ axis. Finally, the symbols indicate that a large portion of the separator is approximately coplanar in the plane defined by κ_{MHD}, particularly at the nose of the magnetosphere where the deviation from the plane is ≤ 0.2 R_E. The deviation is larger near the nulls ($\simeq 1.5$ R_E), which can clearly be seen in Figure 8b, where the ends of the separators flare toward the dawn and dusk flanks. This implies that it is not accurate to model separators as lying in the plane of the nulls.

4.2.3. Comparison With Vacuum Superposition

[39] To gain perspective on the observed trends in separators in MHD simulations with varying IMF clock angle, we compare them to vacuum superposition separators, although a perfect correlation is not expected. As discussed earlier,

MHD separators are mostly coplanar; the vacuum superposition separators are exactly coplanar. Also, the shape of the separator is different between the models. In vacuum superposition, the separator is a circular arc with radius r_{Null} given by equation (6). The MHD separators exhibit the well-known bullet shape of the magnetopause, as seen in Figure 9.

[40] The separator tilt angle dependence on IMF clock angle is displayed in Figure 10. The black pluses display κ_{MHD} as calculated by equation (12). For the vacuum superposition separators, *Yeh* [1976] and *Hu et al.* [2009] showed that the separator tilt angle satisfies $\kappa_{VS} = 90° - \lambda_{Null}$, with λ_{Null} given by equation (7), displayed as the dashed (blue) line. Lastly, the solid (red) line shows $\kappa = \theta_{IMF}/2$, the angle bisecting the IMF and terrestrial magnetic field, a commonly used estimate, for reference.

[41] The separator tilt angle κ increases from 0° to 90° for vacuum superposition, MHD, and angle of bisection. The tilt angles for the three κ values are relatively close to each other, within about 20°. However, quantitative predictions and trends with clock angle reveal important differences between the models. In vacuum superposition, the tilt angle is consistently larger than the angle of bisection, implying separators that are tilted toward the ecliptic plane. MHD separators are tilted toward the noon-midnight meridional plane for $\theta_{IMF} \leq 90°$ but are tilted toward the ecliptic for $\theta_{IMF} = 120°$ and 150°. Therefore, the three models follow similar trends at small and large IMF clock angles, but the MHD separator tilt angle displays significant differences from the models for intermediate clock angles.

4.2.4. Density Dependence of Separators

[42] As a preliminary test of the parametric dependence of MHD separator characteristics, we perform a simulation similar to our $\theta_{IMF} = 30°$ simulation, only changing solar wind number density to $n = 5$ cm^{-3} (from $n = 20$ cm^{-3}). We expect the magnetosphere to expand with this decrease in number density. The location of the magnetopause R_{MP} on the x axis occurs approximately where the solar wind dynamic pressure balances the magnetosphere's magnetic pressure. As the magnetospheric magnetic field is dipolar with $B_D \propto 1/r^3$, the magnetopause location R_{MP} depends on density as $R_{MP} \propto n^{-1/6}$. For these simulations, this implies the magnetopause should approximately expand by a factor of $(5/20)^{-1/6} \simeq 1.26$. The measured values of R_{MP} from the simulations are 9.94 R_E for $n = 5$ cm^{-3} and 8.32 R_E for $n = 20$ cm^{-3}, giving a ratio of $\simeq 1.20$, in good agreement with expectations.
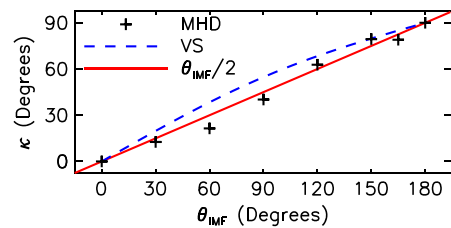
Figure 10. Separator tilt angle κ at the subsolar point as a function of IMF clock angle θ_{IMF}. The solid (red) line is the bisection angle $\theta_{IMF}/2$, the dashed (blue) line is for vacuum superposition separators, and the pluses are for MHD separators.

[43] The magnetic nulls of the $n = 5$ cm^{-3} simulation are located at $\mathbf{r}_{\text{Null}} = (0.56, \pm3.16, \pm11.30)$ R_E. The magnetic nulls of the lower density run are sunward and radially outward from their high density counterparts. This behavior is due to the expansion of the magnetosphere with a lower solar wind density. Thus, the magnetic null locations are sensitive to the solar wind density.

[44] The expansion of the magnetosphere also affects separator location. Figure 9b displays the separators for the two simulations rotated into the principle plane of the separator. The original high density run is displayed as (black) pluses and the low density run as (blue) X's. As expected, the $n = 5$ cm^{-3} separator expands outward in the x'–z' plane. We measure the separator tilt angle using equation (12); the $n = 5$ cm^{-3} run has $\kappa_{\text{MHD}} \simeq 12.9°$ and $n = 20$ cm^{-3} has $\kappa_{\text{MHD}} \simeq 12.6°$. Interestingly, despite the expansion of the magnetosphere changing the separator's location, the separator's tilt angle is not strongly dependent on solar wind number density (for the chosen set of simulation parameters). A more complete parametric study to obtain trends in separator morphology is necessary.

4.2.5. Dependence on Grid Resolution

[45] The null locations given in Table 1 for small and large IMF clock angle exist near or outside the specified high-resolution grid region given in section 3. We test the dependence of the nulls and separators on grid resolution by performing additional simulations with $\theta_{\text{IMF}} = 60°$, $150°$, and $165°$. The same simulation parameters described in section 3 are used, except the 0.125 R_E resolution region with $\theta_{\text{IMF}} = 60°$ spans $-6 < x < 10$, $-10 < y < 10$, $-12 < z < 12$ R_E and $-6 < x < 10$, $-15 < y < 15$, $-10 < z < 10$ R_E for the two southward IMF simulations.

[46] The nulls in the higher resolution simulations are located at $\mathbf{r}_{\text{Null}} = (-0.19, \pm5.23, \pm9.63)$ R_E for $60°$, $\mathbf{r}_{\text{Null}} = (-1.58, \pm11.12, \pm3.20)$ R_E for $150°$, and $\mathbf{r}_{\text{Null}} = (0.30, \pm10.62, \pm2.12)$ R_E for $165°$. The nulls in the higher resolution simulations are $\simeq 3$ high-resolution grid cells away from their lower resolution counterparts for $60°$, $\simeq 5$ high-resolution grid cells for $150°$, and $\simeq 7$ high-resolution grid cells for $165°$. The location of the subsolar point (as measured by the last closed field line on the x axis) is $x = 8.62$ R_E in the $60°$ higher resolution simulation, compared to $x = 8.44$ R_E for the lower resolution simulation, a difference of about 1.5 grid cells; the last closed field lines for $150°$ and $165°$ are within a grid cell of their lower resolution counterparts. We trace separators in all higher resolution simulations and find that the separators in the higher resolution simulations do not deviate significantly from the lower resolution separators (not shown). This motivates that the resolution is sufficient to obtain accurate null locations and separators.

5. Conclusions

[47] In summary, we present a simple, efficient, and accurate method of tracing magnetic separators in global magnetospheric simulations with arbitrary IMF clock angle. The method is to start at a magnetic null and iteratively trace the dayside separator by calculating the magnetic topology on the surface of spherical shells to locate regions of topological merging. We verify the method using a simple magnetic field model with exact solutions for the separators. The technique improves on previous ones by being efficient, good to arbitrary accuracy, and works for any IMF clock angle.

[48] We then trace separators in several distinct resistive global MHD simulations with θ_{IMF} ranging from $0°$ to $180°$. The resulting magnetic nulls and separators in MHD are compared to those in vacuum superposition. We find that the y and z coordinates of the magnetic nulls display similar qualitative trends in both models, but the migration of the null's x coordinate in MHD is not captured by the vacuum superposition fields. We find that the method described here can trace MHD separators for arbitrary clock angle, whereas the last closed field line on the Sun-Earth line only works for northward IMF in our simulations. MHD separators maintain a similar shape regardless of IMF clock angle and a large portion of the separators are approximately coplanar; however, this plane does not contain the nulls. We find that both models have separators that change orientation without appreciably changing shape much. However, trends within models differ significantly. A preliminary test of the separator's dependence on solar wind number density n reveals that the null locations and separator location do depend on number density, but separator orientation does not strongly depend on number density for our chosen solar wind parameters.

[49] The present study has focused on the dayside magnetopause, but it could be useful in other contexts. *Xiao et al.* [2006, 2007] observed magnetic nulls and separators at Earth's nightside, and it is plausible that the method described here could locate separators at the nightside. The method described in the present study could also be used in studies of the solar corona and other planetary magnetospheres.

[50] The results here could assist satellites locate magnetic reconnection at the dayside magnetopause. This would be of particular interest to NASA's upcoming Magnetospheric Multiscale (MMS) mission and other existing missions studying magnetic reconnection at the dayside magnetopause.

[51] This work employed several simplifying assumptions. The present study included an explicit resistivity to limit the effect of numerical dissipation. However, this is inappropriate for realistic modeling of Earth's magnetosphere. It would be interesting and important in future work to find separators in simulations with more realistic collisionless dissipation, such as global Hall-MHD or hybrid simulations, and compare them to the separators in resistive MHD simulations.

[52] We constructed our simulations to not have flux transfer events (FTEs) [*Russell and Elphic*, 1978]. *Dorelli and Bhattacharjee* [2008, 2009] showed that the separator splits into multiple branches in the presence of FTEs at the dayside magnetopause. In order to trace separators in simulations with FTEs, the presently described method would need to be modified to allow for multiple separator branches on a hemisphere's surface and then trace each branch separately. This implementation is relatively straightforward and will be the subject of a future study.

[53] We also assume a quasi-steady state with our choice of constant and uniform solar wind parameters. We look at the magnetic separators late in simulation time after the magnetopause has achieved a steady state. *Laitinen et al.* [2007]

rotated the IMF by 10° every 10 min and found that the magnetic separators exhibit a form of hysteresis.

[54] We have parametrized the magnetic nulls and separators for a small subset of solar wind conditions, with particular emphasis on IMF clock angle. A future study should parametrize the magnetic nulls and separators as a function of solar wind conditions, dipole tilt, and IMF B_x to develop a predictive capability.

References

Angelopoulos, V., et al. (2008), Tail reconnection triggering substorm onset, *Science*, *321*, 931–935.

Borovsky, J. E. (2008), The rudiments of a theory of solar wind/magnetosphere coupling derived from first principles, *J. Geophys. Res.*, *113*, A08228, doi:10.1029/2007JA012646.

Burch, J. L., and J. F. Drake (2009), Reconnecting magnetic fields, *Am. Sci.*, *97*, 392–399.

Cassak, P. A., and M. A. Shay (2007), Scaling of asymmetric magnetic reconnection: General theory and collisional simulations, *Phys. Plasmas*, *14*, 102114, doi:10.1063/1.2795630.

Cassak, P. A., and M. A. Shay (2009), Structure of the dissipation region in fluid simulations of asymmetric magnetic reconnection, *Phys. Plasmas*, *16*, 055704, doi:10.1063/1.3086867.

Close, R. M., C. E. Parnell, and E. R. Priest (2004), Separators in 3D quiet-sun magnetic fields, *Solar Phys.*, *225*, 21–46.

Cowley, S. W. H. (1973), A qualitative study of the reconnection between the Earth's magnetic field and an interplanetary field of arbitrary orientation, *Radio Sci.*, *8*(11), 903–913.

De Zeeuw, D., T. Gombosi, C. Groth, K. Powell, and Q. Stout (2000), An adaptive MHD method for global space weather simulations, *IEEE T. Plasma Sci.*, *28*, 1956–1965.

Dorelli, J. C., and A. Bhattacharjee (2008), Defining and identifying three-dimensional magnetic reconnection in resistive magnetohydrodynamic simulations of Earth's magnetosphere, *Phys. Plasmas*, *15*, 056504, doi:10.1063/1.2913548.

Dorelli, J. C., and A. Bhattacharjee (2009), On the generation and topology of flux transfer events, *J. Geophys. Res.*, *114*, A06213, doi:10.1029/2008JA013410.

Dorelli, J. C., M. Hesse, M. M. Kuznetsova, L. Rastaetter, and J. Raeder (2004), A new look at driven magnetic reconnection at the terrestrial subsolar magnetopause, *J. Geophys. Res.*, *109*, A12216, doi:10.1029/2004JA010458.

Dorelli, J. C., A. Bhattacharjee, and J. Raeder (2007), Separator reconnection at Earth's dayside magnetopause under generic northward interplanetary magnetic field conditions, *J. Geophys. Res.*, *112*, A02202, doi:10.1029/2006JA011877.

Dungey, J. W. (1961), Interplanetary magnetic field and the auroral zones, *Phys. Rev. Lett.*, *6*, 47–48.

Dungey, J. W. (1963), The structure of the exosphere, or adventures in velocity space, in *Geophysics: The Earth's Environment*, edited by C. De Witt et al., pp. 505–550, Gordon Breach, New York.

Gombosi, T., D. DeZeeuw, C. Groth, and K. Powell (2000), Magnetospheric configuration for Parker-spiral IMF conditions: Results of a 3D AMR MHD simulation, *Adv. Space Res.*, *26*, 139–149.

Gonzalez, W. (1990), A unified view of solar wind-magnetosphere coupling functions, *Planet. Space Sci.*, *38*(5), 627–632.

Greene, J. M. (1988), Geometrical properties of three-dimensional reconnecting magnetic fields with nulls, *J. Geophys. Res.*, *93*, 8583–8590.

Haynes, A. L., and C. E. Parnell (2007), A trilinear method for finding null points in a three-dimensional vector space, *Phys. Plasmas*, *14*, 082107, doi:10.1063/1.2756751.

Haynes, A. L., and C. E. Parnell (2010), A method for finding three-dimensional magnetic skeletons, *Phys. Plasmas*, *17*, 092903, doi:10.1063/1.3467499.

Haynes, A. L., C. E. Parnell, K. Galsgaard, and E. R. Priest (2007), Magnetohydrodynamic evolution of magnetic skeletons, *Proc. R. Soc. A*, *463*, 1097–1115.

Hu, Y. Q., Z. Peng, C. Wang, and J. R. Kan (2009), Magnetic merging line and reconnection voltage versus IMF clock angle: Results from global MHD simulations, *J. Geophys. Res.*, *114*, A08220, doi:10.1029/2009JA014118.

Laitinen, T. V., P. Janhunen, T. I. Pulkkinen, M. Palmroth, and H. E. J. Koskinen (2006), On the characterization of magnetic reconnection in global MHD simulations, *Ann. Geophys.*, *24*, 3059–3069.

Laitinen, T. V., M. Palmroth, T. I. Pulkkinen, P. Janhunen, and H. E. J. Koskinen (2007), Continuous reconnection line and pressure-dependent energy conversion on the magnetopause in a global MHD model, *J. Geophys. Res.*, *112*, A11201, doi:10.1029/2007JA012352.

Lau, Y.-T., and J. M. Finn (1990), Three-dimensional kinematic reconnection in the presence of field nulls and closed field lines, *Astrophys. J.*, *350*, 672–691.

Liu, Z.-Q., J. Y. Lu, K. Kabin, Y. F. Yang, M. X. Zhao, and X. Cao (2012), Dipole tilt control of the magnetopause for southward IMF from global magnetohydrodynamic simulations, *J. Geophys. Res.*, *117*, A09237, doi:10.1029/2011JA017441.

Longcope, D. W. (1996), Topology and current ribbons: A model for current, reconnection and flaring in a complex, evolving corona, *Solar Phys.*, *169*, 91–121.

Lu, J. Y., Z.-Q. Liu, K. Kabin, M. X. Zhao, D. D. Liu, Q. Zhou, and Y. Xiao (2011), Three dimensional shape of the magnetopause: Global MHD results, *J. Geophys. Res.*, *116*, A07207, doi:10.1029/2010JA016418.

Moore, T., J. Burch, W. Daughton, S. Fuselier, H. Hasegawa, S. Petrinec, and Z. Pu (2013), Multiscale studies of the three-dimensional dayside x-line, *J. Atmos. Sol. Terr. Phys.*, *99*, 32–40, doi:10.1016/j.jastp.2012.10.004.

Moore, T. E., M.-C. Fok, D. C. Delcourt, S. P. Slinker, and J. A. Fedder (2008), Plasma plume circulation and impact in an MHD substorm, *J. Geophys. Res.*, *113*, A06219, doi:10.1029/2008JA013050.

Ouellette, J. E., B. N. Rogers, M. Wiltberger, and J. G. Lyon (2010), Magnetic reconnection at the dayside magnetopause in global Lyon-Fedder-Mobarry simulations, *J. Geophys. Res.*, *115*, A08222, doi:10.1029/2009JA014886.

Parnell, C. E., J. M. Smith, T. Neukirch, and E. R. Priest (1996), The structure of three-dimensional magnetic neutral points, *Phys. Plasmas*, *3*, 759–770.

Powell, K. G., P. L. Roe, T. J. Linde, T. I. Gombosi, and D. L. D. Zeeuw (1999), A solution-adaptive upwind scheme for ideal magnetohydrodynamics, *J. Comp. Phys.*, *154*, 284–309.

Raeder, J. (1999), Modeling the magnetosphere for northward interplanetary magnetic field: Effects of electrical resistivity, *J. Geophys. Res.*, *104*, 17357–17367.

Russell, C. T., and R. C. Elphic (1978), Initial ISEE magnetometer results: Magnetopause observations, *Space Sci. Rev.*, *22*, 681–715.

Siscoe, G. L. (1987), The magnetospheric boundary, in *Physics of Space Plasmas*, edited by T. Chang, G. B. Crew, and J. R. Jasperse, pp. 3–78, Scientific, Cambridge, Mass.

Siscoe, G. L., G. M. Erickson, B. U. Ö. Sonnerup, N. C. Maynard, K. D. Siebert, D. R. Weimer, and W. W. White (2001), Global role of $E_\parallel$ in magnetopause reconnection: An explicit demonstration, *J. Geophys. Res.*, *106*, 13015–13022.

Siscoe, G. L., G. M. Erickson, B. U. Ö. Sonnerup, N. C. Maynard, J. A. Schoendorf, K. D. Siebert, D. R. Weimer, W. W. White, and G. R. Wilson (2002), Flow-through magnetic reconnection, *Geophys. Res. Lett.*, *29*(13), doi:10.1029/2001GL013536.

Xiao, C. J., et al. (2006), In situ evidence for the structure of the magnetic null in a 3D reconnection event in the Earth's magnetotail, *Nat. Phys.*, *2*, 478–483.

Xiao, C. J., et al. (2007), Satellite observations of separator-line geometry of three-dimensional magnetic reconnection, *Nat. Phys.*, *3*, 609–613.

Yeh, T. (1976), Day side reconnection between a dipolar geomagnetic field and a uniform interplanetary field, *J. Geophys. Res.*, *81*, 2140–2144.